

# Local friction at a sliding interface between an elastomer and a rigid spherical probe

A. Chateauinois<sup>a</sup> and C. Fretigny<sup>b</sup>

Laboratoire de Physico-Chimie des Polymères et des Milieux Dispersés (PPMD), UMR CNRS 7615, Université Pierre et Marie Curie (UPMC), Ecole Supérieure de Physique et Chimie Industrielles (ESPCI), 10 rue Vauquelin, 75231 Paris Cedex 05, France

Received 18 July 2008

Published online: 15 October 2008 – © EDP Sciences / Società Italiana di Fisica / Springer-Verlag 2008

**Abstract.** This paper reports on spatially resolved measurements of the shear stress distribution at a frictional interface between a flat rubber substrate and a glass lens. Silicone rubber specimens marked close to their surface by a colored pattern have been prepared in order to measure the surface displacement field induced by the steady-state friction of the spherical probe. The deconvolution of this displacement field then provides the actual shear stress distribution at the contact interface. When a smooth glass lens is used, a nearly constant shear stress is achieved within the contact. On the other hand, a bell-shaped shear stress distribution is obtained with rough lenses. These first results suggest that simple notions of real contact area and constant interface shear stress cannot account for the observed changes in local friction when roughness is varied.

**PACS.** 46.55.+d Tribology and mechanical contacts – 62.20.Qp Friction, tribology, and hardness

## 1 Introduction

Despite long-standing efforts, mechanisms of friction remain partially unsolved. As adhesive static contact problems, friction couples mechanical properties of the materials, roughness and physical-chemistry of their surfaces. It also involves dynamical processes which are not clearly understood. Recent developments of static contact mechanics [1–4] allow to better understand adhesion and roughness effects. However, to transpose them to friction situations, it is necessary to postulate a local constitutive relation indicating how shear stress depends on normal stress at the interface. This local friction law contains the physics of the frictional interaction between two ideally flat contacting units of area. It involves interesting, although poorly understood, physical-chemistry processes occurring at a molecular level, like adsorption or entanglement/disentanglements mechanisms [5, 6] for instance.

Bowden and Tabor [7], and later Greenwood and Williamson [8] were the first to propose such descriptions. Their interpretation is based on the observation that the contact between two macroscopic solids is generally made up of a large number of micro-contacts at which the two solids interact with one another at a molecular level: The real area of contact is thus smaller than the macroscopically apparent one due to the distribution of the asperities

height on the surfaces. Several models were then proposed for evaluating the real area using a more refined description of the surface roughness represented by their two-points height difference correlations [1, 3]. This concept of real contact area is central to sliding situations where the overall friction force is usually assumed to be the sum of the shear resistance of individual micro-contacts.

As a crude approximation, a constant shear stress can be ascribed to local friction processes at the micro-contacts level. When incorporated into the Greenwood and Williamson model, such a constant shear stress hypothesis provides a theoretical background for the well-known Coulomb's friction law. More refined descriptions introduced by Briscoe and Tabor [9] sometimes take into account a linear pressure dependence term. Although the original Bowden and Tabor model has been modified over the years in order to account for rate dependence or ageing effects on friction, it remains the current framework for the description of solid friction at multicontact interfaces (see, *e.g.*, [10] for a review). Unfortunately, most experiments only rely on the measurements of the friction force and of its dependence on load and velocity, which are average quantities of local frictional properties. Then, validation of the local friction laws, and, *a fortiori*, of the proposed models, remains rather undirect.

In this paper, we describe a method which allows for the determination of the distribution of the interfacial friction in a contact between a rigid sphere and a flat rubber sample. The approach is based on the measurement of

<sup>a</sup> e-mail: antoine.chateauinois@espci.fr

<sup>b</sup> e-mail: christian.fretigny@espci.fr

the friction-induced surface displacements by means of *in situ* contact visualisation. Imagery of surfaces has been recently used in the context of mechanics problems [11–13], where digital image correlation techniques were found to allow for an accurate determination of the displacement fields in static situations. Here, this field is deduced from the displacement of characteristic features at the surface of the rubber sample in a steady friction regime, in the spirit of early experimental works by Schallamach [14] and Barquins and Courtel [15]. In his experiments, Schallamach used a transparent rubber sheet marked with a square lattice to discuss qualitatively the distribution of surface strains induced by the sliding of a glass sphere. A similar technique was used in a slightly different and more quantitative way by Barquins and Courtel [15] to determine the distribution of the displacement along the central symmetry axis of the contact. Tangential displacements were measured from the distortion of a straight line traced on the surface, perpendicular to the direction of motion and passing through the contact zone. These measurements were used to discuss the tensile and compressive nature of the longitudinal surface strain. In the present study, a complete surface displacement field is measured within the contact zone from the deformation of a square lattice on the surface of the rubber substrate. Then, the corresponding shear stress distribution is obtained via a deconvolution technique. It can be noted in passing that similar deconvolution approaches were recently applied in a different context to the determination of the mechanical forces exerted by moving cells on flexible substrates [16–18]. In the present work, deconvolution is used to investigate friction of a rubber against a glass sphere. Experimental investigations on that topic have been largely concentrated on instabilities such as the so-called Schallamach detachment waves [14, 19–21] or stick-slip motions [22]. Here, we focus on the steady-state friction regime which has been the object of a more limited number of investigations since the seminal work by Grosh [23].

## 2 Experimental details

The friction experiments were carried out using a commercially available poly(dimethylsiloxane) (PDMS) silicone elastomer (Sylgard 184, Dow Chemical). In order to monitor friction-induced surface displacements, each specimen was marked with a squared colored grid which was embedded a few micrometers beneath the surface in order not to modify frictional properties. The spacing between the lines of the grid was set to  $400\ \mu\text{m}$ . As schematically depicted in Figure 1, the grids were realized using micro-lithography techniques. In a first step, squared patterns of micro-channels  $16\ \mu\text{m}$  in depth and  $20\ \mu\text{m}$  in width were produced on the surface of PDMS specimens by directly molding the silicon reactive mixture onto a resin template. The latter was realized by means of photo-lithography techniques on a silicon wafer.

After polymerization and demolding of the PDMS sample, the surface imprint was filled with a solution of rhodamine in isopropanol. When complete evaporation of

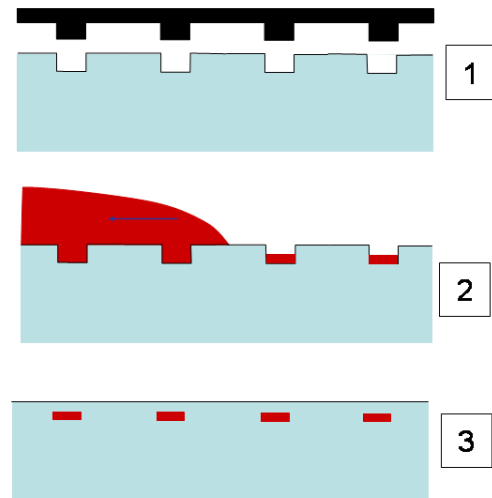


**Fig. 1.** Schematic description of the realization of the (on line) colored grids close to the surface of the PDMS specimens. (1) Molding of the PDMS specimen onto a resin template. (2) Deposition of the rhodamine die by evaporation from a solution in isopropanol. (3) Deposition and crosslinkage of a thin (about  $15\ \mu\text{m}$ ) layer of PDMS on the top surface of the marked substrate.

the isopropanol solvent was achieved, the colored lattice was covered with a thin layer (about  $15\ \mu\text{m}$ ) of PDMS in order to produce a smooth surface and to avoid any contact between the rhodamine die and the sliding probe. At both stages of this process, the silicon monomer and the hardener were mixed in a 10:1 weight ratio and crosslinked at room temperature for one week. The thickness of the PDMS specimens was  $15\ \text{mm}$  and their lateral dimensions  $20 \times 40\ \text{mm}$ .

Friction experiments were carried out using a home-made device. The experimental setup is similar to the one described in [24], with a higher force measurement sensitivity and larger possible displacements. Contacts were achieved between the PDMS specimens and a plano-convex BK7 glass lens (Melles Griot, France) with a radius of curvature of  $9.3\ \text{mm}$ . The r.m.s. roughness of the as received lens was less than  $2\ \text{nm}$ , as measured by optical interferometry. Alternatively, the glass lens was sanded with silica powder. From AFM analysis of the surface, a roughness of about  $1\ \mu\text{m}$  is found on an area of  $100 \times 100\ \mu\text{m}^2$ . The power spectral density has a power law shape (with an exponent of about 3.5) in the range  $50\ \text{nm}$ – $30\ \mu\text{m}$ . Linear sliding experiments were performed under imposed normal load (between  $1.2\ \text{N}$  and  $3.0\ \text{N}$ ) and velocity (between  $0.01$  and  $1\ \text{mm/s}$ ). The PDMS substrate was displaced with respect to the fixed glass lens by means of a linear translation stage. Under steady-state sliding, images of the deformed contact zone were continuously recorded through the transparent PDMS substrate using a zoom, a CCD camera and a frame grabber. This system was configured to a frame size of  $(512 \times 512)$  pixels with frame rates ranging from  $1\ \text{Hz}$  to  $25\ \text{Hz}$ . In addition, the lateral force was measured by means of a  $25\ \text{N}$  strain gage transducer (Entran, France).

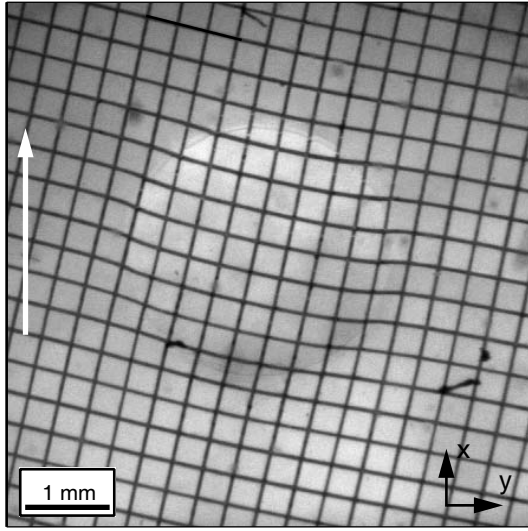


**Fig. 2.** Image of the deformed contact zone under steady-state friction ( $v = 0.1$  mm/s). The displacement direction of the PDMS substrate is indicated by the white arrow. The grid has been on purpose slightly disoriented with respect to the sliding direction (see text for explanations).

### 3 Determination of stress and displacement fields

The measurement of the displacement field was based on the detection of the location of the nodes of the grid by means of image processing. As detailed above, the spherical lens was fixed with respect to the CCD camera while the PDMS specimen was continuously translated during sliding. Under steady-state friction, it was therefore possible to record sequences of images where the PDMS grid was progressively translated with respect to the fixed contact. If care is taken to slightly disorient the grid with respect to the sliding direction (Fig. 2), it comes out that many data points can be accumulated during a single experiments. They are densely and almost uniformly distributed within the observation frame. As an indication, the analysis of a series of 200 images yield about  $10^5$  data points in the field of view.

In order to determine the friction-induced surface displacements, two synchronous series of images were successively acquired: a reference one where the grid was moved without contact and a second one with a frictional contact under identical velocity conditions. From a comparison between these two sets of images, in-plane displacements components  $u_x$  and  $u_y$  were determined. Directions  $x$  and  $y$  are, respectively, parallel and perpendicular to the direction of sliding. Figure 3 shows a typical example of the obtained displacement fields (note that the color scale for  $u_y$  has been magnified by a factor of twenty as compared to that for  $u_x$ ). An odd symmetry with respect to the center of the contact is achieved for the  $u_y$  component: surface displacements are oriented outward at the leading edge of the contact and inward at the trailing edge, which may be viewed as the manifestation of the “flow” of the silicone elastomer around the sliding sphere.

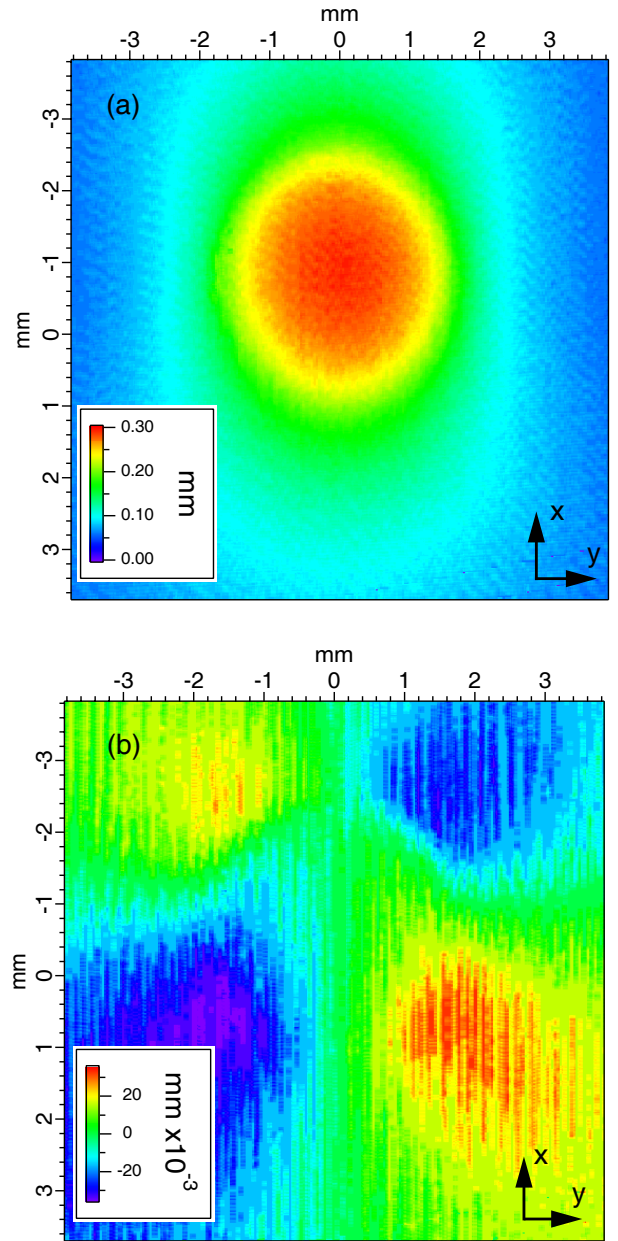


**Fig. 3.** (Colour on-line) Measured displacement field under steady-state sliding ( $v = 0.1$  mm/s). The displacement components are measured (a) in the direction of sliding ( $u_x$ ) and (b) perpendicular to the sliding direction ( $u_y$ ). The PDMS substrate is displaced from bottom to top with respect to fixed glass lens. Note that the color scale for  $u_y$  has been magnified by a factor of twenty as compared to that for  $u_x$ .

These displacement fields can be used to obtain the corresponding distribution of the surface shear stress. The basis for this inversion is the so-called Green’s tensor which provides the expressions for the displacements induced within a semi-infinite elastic body by a point loading applied to the surface [25]. In the case of incompressible materials such as rubber, Green’s analysis establishes that the displacements induced by the vertical and lateral components of the point loading are fully decoupled.

As a consequence, the surface displacement components  $u_x$  and  $u_y$  can be expressed as a function of the lateral components,  $F_x$  and  $F_y$ , of the point loading only

$$\begin{bmatrix} u_x \\ u_y \end{bmatrix} = \frac{3}{4\pi E} \begin{bmatrix} G_{xx} & G_{xy} \\ G_{yx} & G_{yy} \end{bmatrix} \begin{bmatrix} F_x \\ F_y \end{bmatrix}, \quad (1)$$

where  $E$  is Young's modulus. The functions  $G_{ij}$  are the Green's tensor components defined as follows:

$$G_{xx} = \frac{1}{r} + \frac{x^2}{r^3}, \quad (2)$$

$$G_{xy} = G_{yx} = \frac{xy}{r^3}, \quad (3)$$

$$G_{yy} = \frac{1}{r} + \frac{y^2}{r^3}. \quad (4)$$

If these expressions for a point loading are extended to a distribution of surface tractions, it comes out that the lateral surface displacement field can be expressed as a convolution of the surface shear stresses by the Green's functions

$$u_i = G_{ij} * \sigma_{jz}. \quad (5)$$

In this expression, subscripts  $i$  and  $j$  stand for  $x$  or  $y$ . As mentioned above, in plane displacements are not coupled with the normal pressure  $\sigma_{zz}$ . Deconvolution problems are ill-posed and cannot be performed directly by Fourier transform. Alternatively, a classical Van Cittert iterative algorithm [26] was implemented. At each computational step, this algorithm consists in adding to the previously computed stress field,  $\sigma_{iz}^n$ , a corrective term which is proportional to the difference between the experimental values of the displacements,  $u_{\text{exp}}$ , and the calculated ones at step  $n$ ,

$$\sigma_{iz}^{n+1} = \sigma_{iz}^n + m (G_{ij} * \sigma_{jz}^n - u_i^{\text{exp}}), \quad (6)$$

where  $m$  is a numerical "relaxation" parameter. When applying such an iterative deconvolution procedure to experimental data, it is often necessary to incorporate some additional constraints into the algorithm in order to ensure convergence. In the present case, such constraints were found to be unnecessary as the displacement field was very densely sampled with a high signal-to-noise ratio. In particular, it must be emphasized that no constraint was added regarding the location of the contact area. The initial stress components were taken to be proportional to the corresponding displacement fields. A relaxation factor,  $m = 10^8 \text{ N m}^{-3}$ , was empirically found to be adequate to ensure convergence in about 30 iterations. The latter was verified from a comparison between the experimental and calculated displacements (Fig. 4).

The application of such a deconvolution procedure to the displacement field implies that the substrate deformation remains within the linear elastic range. As a first approximation, a typical strain of 0.11 can be deduced from the ratio of the contact radius to the radius of curvature of the lens. A more precise determination of the surface strains can also be obtained from a derivation of the measured displacements field. It confirms that the surface

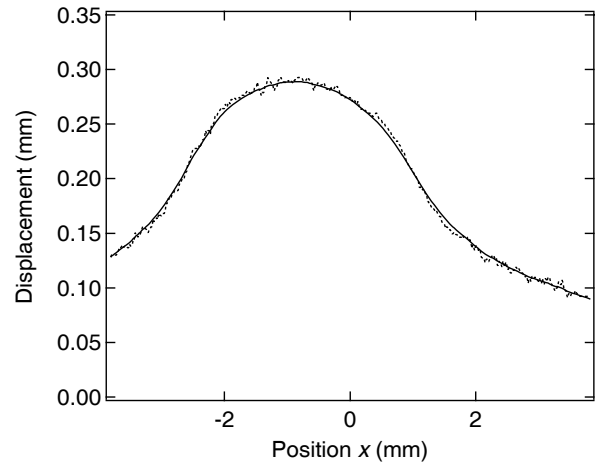


**Fig. 4.** Comparison between the measured and the calculated values of the displacement at the end of the inversion procedure. The profiles correspond to a cross-section of the longitudinal displacement ( $u_x$ ) field along a line parallel to the sliding trajectory and passing through the center of the contact ( $x$ -direction). Solid line: calculated displacement obtained from the convolution (Eq. (5)) of the Green tensor by the stress field obtained at the end of the inversion; dotted line: measured displacement. The PDMS substrate is displaced from left to right with respect to the fixed glass lens.

strains did not exceed 10 percent. Within this range, the PDMS substrate can be considered as linear elastic [27]. Its Young's modulus was determined from lateral contact measurements using a procedure fully detailed in references [24, 28] and briefly recalled here. When lateral displacements low enough are applied to a contact, one can neglect slip and describe the friction experiment as the drag of a circular region of the sample surface by the slider. The amplitude of the load response,  $F_t$  is then linearly related to the displacement amplitude  $\delta$  through the tangential stiffness  $K_t = F_t/\delta$ . In the case of an incompressible substrate,  $K_t$  can be related to the shear modulus of the substrate,  $G$ , using the following expression [29]:

$$K_t = \frac{16}{3}Ga, \quad (7)$$

where  $a$  is the contact radius. Using this method, Young's modulus of the substrate,  $E = 3G$  was found to be 1.5 MPa.

Figure 5 shows an example of the resulting distributions of the surface shear stress  $\sigma_{xz}$  and  $\sigma_{yz}$ . The stress component,  $\sigma_{yz}$ , perpendicular to the sliding direction was found to be negligible as compared to  $\sigma_{xz}$ ; the shear stress is essentially oriented along the sliding direction.

It can be noted in passing that the same deconvolution approach could also be applied independently to the determination of the normal contact stress  $\sigma_{zz}$ . As the Poisson ratio of the rubber substrate is 0.5, decoupling between normal and lateral stress components imposes that  $u_z = G_{zz} * \sigma_{zz}$ , where  $u_z$  is the vertical surface displacement and  $G_{zz} = 1/r$  [25]. Deconvolution of this expression would require that vertical displacements are

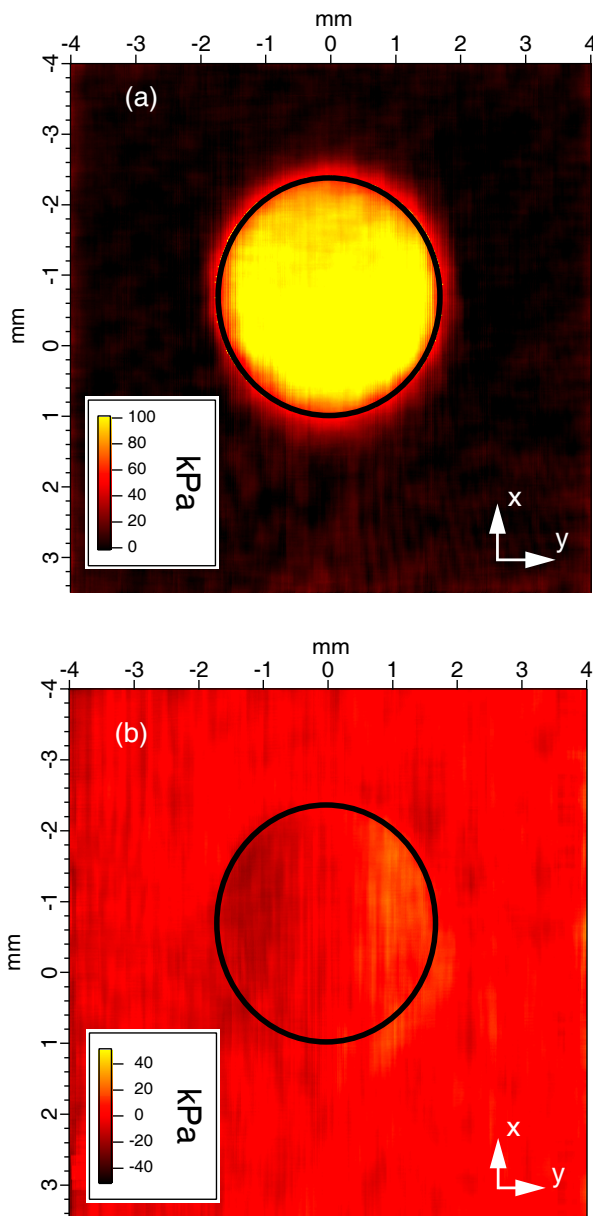


**Fig. 5.** (Colour on-line) Calculated shear stress distribution at the surface of the PDMS specimen under steady-state sliding ( $v = 0.1$  mm/s). The stress components are determined (a) along the sliding direction ( $\sigma_{xz}$ ); (b) perpendicular to the sliding direction ( $\sigma_{yz}$ ). The PDMS substrate is displaced from bottom to top. The black contours delimit the contact zone in the undeformed space (see text for details).

known, which is not directly the case. However, as the shape of the indenter and the contact shape are known, vertical displacements may be deduced up to a rigid displacement. Then normal stress could be obtained by another deconvolution procedure if one supposes that they do not diverge at the edge of the contact (the situation is analogous if we compare Hertz and adhesive JKR contacts [30]). This has not been done in the present study but will be the subject of a forthcoming investigation.

## 4 Results and discussion

To assess the quality of the procedure described in the above section, one may check that the calculated stresses are zero out of the contact zone. This region can be precisely known by using the different images of the surface acquired during the experiment. By averaging all these images, the grid is blurred out revealing the contact zone as a lighter region. Then, as the stress distribution is calculated in the unstrained space, we use the displacement field which has been measured to calculate the shape of the boundary of the contact region in the undeformed plane. This line is superimposed to the longitudinal stress distribution in Figure 5. It is apparent from this figure that the regions of non-zero stress are well localized in the contact zone, confirming the quality of their determination, since no assumption was made of the contact shape in the data analysis. It can also be checked that the integration of the obtained interfacial stress is consistent with the measured total friction force.

Cross-sections of the longitudinal stress distribution through a line perpendicular to the trajectory passing through the center are shown in Figure 6 for both a smooth and a rough glass sphere contact. When the glass sphere is smooth the longitudinal stress is remarkably constant in the contact region. This is also clear from Figure 5 where the intensity of the stress is almost constant in the contact region. The situation is very different in the case of a rough sphere: the stress distribution has a bell shape. As shown in Figure 5, this shape is preserved when the contact load is increased from 1.2 N to 3.0 N but it can be noted that the stress at the center of the contact remains constant. These shear stress distributions remain unchanged when the sliding velocity is varied between 0.01 and 1 mm s<sup>-1</sup>. Such an observation is consistent with the experimental data for other rubber systems which exhibit only a slight variation in friction with rate for temperatures far from the glass transition temperature [19] (the glass transition temperature of PDMS is about -120 °C).

These results may be discussed in the light of the classical Bowden and Tabor approach to friction [7]. As mentioned in the introduction, the contact interface between rough surfaces is formed of a myriad of micro-contacts which are sheared when the surfaces slide over each other. As a first approximation, a constant interfacial strength,  $\sigma_0$ , can be ascribed to each of these micro-junctions. The friction force,  $F$ , is then obtained by summing the contributions of individual micro-contacts, *i.e.*  $F = \sigma_0 A$ , where  $A$  is the actual contact area. Then, the macroscopic friction laws may be retrieved by considering the dependence of the actual contact area on the applied normal load. If, for instance, the Greenwood and Williamson model [8] is considered, it comes out that the actual contact area is proportional to the normal load.

In the current experiments, the intimate macroscopic contact formed between the soft PDMS substrate and the smooth glass lens can be assimilated to a single-asperity contact. In that respect, the constant profile measured for the smooth surface (Fig. 6(a)) shows that interface shear stress is independent of the applied contact pressure.

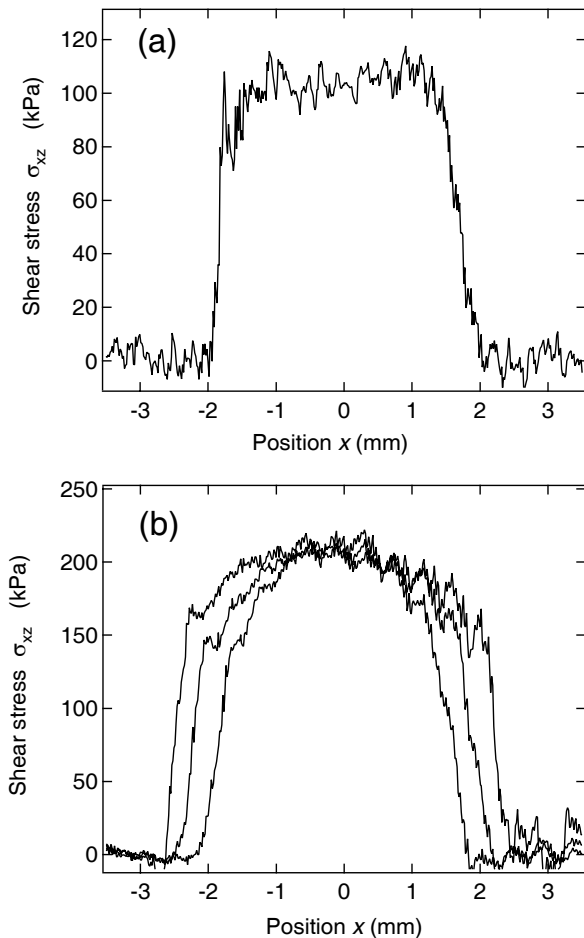


**Fig. 6.** Shear stress distribution within a sliding contact between the PDMS substrate and (a) a smooth and (b) a rough glass lens. These stress profiles correspond to cross-sections of the longitudinal stress ( $\sigma_{xz}$ ) distribution through a line perpendicular to the trajectory passing through the center ( $x$ -direction). The three profiles plotted in (b) correspond, by increasing order of lateral expansion, to the following values of the normal load: 1.2 N, 2.1 N and 3.0 N.

In the case of the rough surface, one can consider that the observed bell shape of the shear stress distribution reflects the dependence of the actual contact area on the normal contact pressure distribution. Accordingly, the constancy of the shear stress at the center of the contact when the applied normal load is varied could be viewed as evidence of a saturation of the micro-contacts density in this area, where the maximum contact pressure is achieved. However, this simple description is contradicted by the observation that the average shear stress measured for the rough surface (about 200 kPa) is about twice that for the smooth surface. The constant shear stress measured for the smooth macroscopic contact can therefore not be reported directly at the micro-asperity level, as one would do following the basic assumption of the Bowden and Tabor model. Viscoelastic dissipation at the micro-asperity scale could be invoked to explain this discrepancy between smooth and rough interfaces. Within the rough interface,

the PDMS surface is locally deformed at a frequency of the order of  $v/d$ , where  $v$  is the sliding velocity and  $d$  is the characteristic size of the asperity. From the topographical analysis of the rough glass lens, this frequency can be estimated to be less than 1 MHz. For the considered low glass transition temperature ( $T_g = -120^\circ\text{C}$ ) PDMS substrate, a significant viscoelastic dissipation is not likely to occur at such frequency. This is further confirmed by the observation that the shear stress distribution within the rough interface was not altered when the sliding velocity is varied between 0.01 and 1 mm/s.

It could also be argued that the sanding treatment may alter the surface chemistry of the glass, thus affecting its interaction with the PDMS. Fresh glass surfaces created during sanding could, for example, exhibit an increased concentration in surface silanol groups which may result in increased hydrogen bonding interactions with the silicone. Chemistry and adhesion effects may thus interfere with purely geometrical effects. However, we checked that the results are very reproducible after several months. If the observed difference between smooth and rough glass surfaces was only due to an increase in the silanol concentration after sanding, this effect would probably disappear after soaking the glass lens several months in ambient conditions, as the silanol groups tend to condense to restore the original siloxane bonds.

More subtle effects need therefore to be considered to account for the differences between the shear stress distributions measured using rough and smooth glass surfaces. This would probably require a more refined analysis of micro-asperity contacts, including potential interactions between neighboring asperities. However, the present results suggest that simple notions of real contact area and constant shear stress cannot fully account for the variation in friction when the surface roughness is varied. It can be noted that such a conclusion presents some similarities with that drawn from a recent study by Scheibert *et al.* [31] in the case of the normal contact of a multicontact interface between a rough PDMS substrate and a smooth glass sphere. From a measurement of the normal stress field, these authors showed that the classical “macroscopic” Amontons’ friction law does not apply locally at the contact interface. This discrepancy was attributed to the finite compliance of the multicontact interface.

## 5 Conclusion

In this study, we have shown that the analysis of friction-induced surface displacements can provide insights into the details of shear stress distribution within sliding interfaces between rubbers and rigid probes. Spatially resolved surface displacement fields have been measured under steady-state friction from the imaging of patterned silicone substrates. Then, an inversion procedure allows for the determination of the corresponding interface shear stress, provided that the response of the rubber substrate remains linear elastic. This experimental approach allows to discuss theoretical friction models. In the case of a smooth

single-asperity macroscopic contact, we showed the existence of a constant shear stress distribution within the contact. However, this simple description cannot be extended to the multicontact interface formed between the silicone substrate and rough glass spheres. In such a situation, the local shear stress is found to be much higher than that expected from simple considerations based on actual contact area and constant shear stress distribution. A better understanding of these effects would probably require a more detailed description of the actual contact conditions between interacting asperities in frictional contacts, which will be the topic of a forthcoming study.

Many thanks are due to Denis Bartolo (PMMH, ESPCI, France) for his kind help and advices during the realization of the patterned silicone specimens. We are also grateful to Alexis Prevost and Georges Debrégeas (LPS, ENS, France) for stimulating discussions.

## References

1. B.N.J. Persson, *J. Chem. Phys.* **115**, 3840 (2001).
2. S. Hyun, M. Robbins, *Tribol. Int.* **40**, 1413 (2007).
3. M.H. Muser, *Phys. Rev. Lett.* **100**, 055504 (2008).
4. B.N.J. Persson, *Surf. Sci. Rep.* **61**, 201 (2006).
5. L. Bureau, L. Leger, *Langmuir* **20**, 4523 (2004).
6. C. Drummond, J. Rodríguez-Hernández, S. Lecommandoux, P. Richetti, *J. Chem. Phys.* **126**, 184906 (2007).
7. F. Bowden, D. Tabor, *The Friction and Lubrication of Solids* (Clarendon Press, Oxford, 1958).
8. J. Greenwood, J. Williamson, *Proc. R. Soc. London, Ser. A, Math. Phys. Sci.* **295**, 1934 (1966).
9. B.J. Briscoe, D. Tabor, *Wear* **34**, 29 (1975).
10. T. Baumberger, C. Caroli, *Adv. Phys.* **55**, 279 (2006).
11. B. Wagne, S. Roux, F. Hild, *Eur. Phys. J. Appl. Phys.* **17**, 247 (2002).
12. F. Hild, S. Roux, *Strain* **42**, 69 (2006).
13. S. Roux, F. Hild, *Int. J. Fract.* **140**, 141 (2006).
14. A. Schallamach, *Wear* **17**, 301 (1971).
15. M. Barquins, R. Courtel, *Wear* **32**, 133 (1975).
16. C. Barentin, Y. Sawada, J. Rieu, *Eur. Biophys. J.* **35**, 328 (2006).
17. J. Rieu, C. Barentin, S. Sawai, Y. Maeda, Y. Sawada, *J. Biol. Phys.* **30**, 345 (2004).
18. U. Schwarz, N. Balaban, D. Riveline, L. Addadi, A. Bershadsky, S. Safran, B. Geiger, *Mater. Sci. Eng. C* **23**, 387 (2003).
19. M. Barquins, A. Roberts, *J. Phys. D: Appl. Phys.* **19**, 547 (1986).
20. B. Best, P. Meijers, A. Savkoor, *Wear* **65**, 385 (1981).
21. G. Briggs, B. Briscoe, *Wear* **35**, 357 (1975).
22. R. Rorrer, *Rubber Chem. Technol.* **73**, 486 (2000).
23. K. Grosh, *Proc. R. Soc. A* **274**, 21 (1963).
24. E. Gacoin, A. Chateauinois, C. Fretigny, *Polymer* **45**, 3789 (2004).
25. L. Landau, E. Lifshitz, *Theory of Elasticity*, Third edition (Butterworth Heinemann, 1986).
26. W. Press, S. Teukolsky, W. Vetterling, B. Flannery, *Numerical Recipes in Fortran*, 2nd edition (Cambridge University Press, 1992).
27. F. Schneider, T. Felner, J. Wilde, U. Wallrabe, *J. Micromech. Microengin.* **18**, DOI 065008 (2008).
28. C. Fretigny, C. Basire, V. Granier, *J. Appl. Phys.* **82**, 43 (1997).
29. R. Mindlin, *ASME Trans., J. Appl. Mech., Ser. E* **16**, 327 (1953).
30. K. Johnson, K. Kendall, A.D. Roberts, *Proc. R. Soc. London, Ser. A* **324**, 301 (1971).
31. J. Scheibert, A. Prevost, J. Frelat, P. Rey, G. Debrégeas, *EPL* **83**, 34003 (2008).